OPEN ACCESS

Analysing Tortuosity for Solid Oxide Fuel Cell Anode Material: Experiments and Modeling

Journal of The Electrochemical Society, 2023 **170** 094502

Analysing Tortuosity for Solid Oxide Fuel Cell Anode Material: Experiments and Modeling

Xiaoqiang Zhang,[1,2,z] Danan Yang,[1] Min Xu,[3] Aaron Naden,[2] Mayken Espinoza-Andaluz,[4] Tingshuai Li,[5] John T. S. Irvine,[2] and Martin Andersson[1,z]

[1]*Department of Energy Sciences, Faculty of Engineering, Lund University, SE-221 00 Lund, Sweden*
[2]*School of Chemistry St Andrews, University of St Andrews, Fife, KY16 9ST, United Kingdom*
[3]*The Future Laboratory, Tsinghua University, Sancaitang building, Haidian District, 100190, Beijing, People's Republic of China*
[4]*Escuela Superior Politécnica del Litoral, ESPOL, Facultad de Ingeniería Mecánica y Ciencias de la Producción, Centro de Energías Renovables y Alternativas, Campus Gustavo Galindo Km. 30.5 Vía Perimetral, P.O. Box 09-01-5863, Guayaquil, Ecuador*
[5]*School of Materials and Energy, University of Electronic Science and Technology of China, West Hi-Tech Zone, 611731, Chengdu, Sichuan, People's Republic of China*

Solid oxide fuel cells (SOFCs) directly convert chemical energy to electricity with high electrical efficiency. It involves gas transport through the porous electrode to the three-phase boundaries (TPB). The tortuosity of gas transport relates the bulk diffusion of gas in free space to the effective diffusion coefficient of gas migrating through a porous material. Therefore, determining the tortuosity is of great importance. This paper tests button SOFCs with NiO-YSZ as anode material followed by dual beam-focused ion beam scanning electron microscopy (FIB-SEM) to obtain 2D serial slice images. Based on processed 2D images and reconstructed 3D microstructure, the tortuosity is calculated using three approaches i.e., porosity-tortuosity correlations, voxel-based, and path-length-based approaches. The test results show that a decrease in Ni content in the anode greatly decreases the cell performance due to a decreased percolated electronic phase. The sample with low performance has high tortuosity. Different approaches vary regarding the tortuosity value and computational time. The path-length-based approach can achieve reasonable accuracy in a relatively short time but is only valid for using the longest path length.
 [DOI: 10.1149/1945-7111/acf884]

Manuscript submitted December 22, 2022; revised manuscript received August 18, 2023. Published September 19, 2023.

Solid oxide fuel cells (SOFCs) have high electrical efficiency and are environmentally friendly with wide applications such as stationary power stations, combined heat and power (CHP) stations, commercial buildings backup power, auxiliary power units (APU) and range extenders.[1,2] However, several obstacles in developing SOFCs need to be addressed, including low performance, short durability, and high cost. Numerous research studies focused on addressing these problems to advance SOFC commercialization. On the one hand, the development of new materials is key to solving these problems, such as the unremitting effort to develop a new type of perovskite materials not only in SOFC but also in many other energy applications.[3] On the other hand, optimisation of the microstructure of the porous electrode is critical to improving the performance and durability of SOFC.[4]

A SOFC cell consists of a dense electrolyte sandwiched by a porous anode and a cathode, where fuel oxidation and oxygen reduction occur separately. The metallic interconnect and ceramic/glass material are needed for a stack for structure support and hermiticity.[5] The anode and cathode material are mixed ionic and electronic conducting phases, increasing the complexity of the electrode. The different phases dominate gas, electron, and ion transport processes. This means that the porous electrode is closely related to electrochemical reactions, transport processes, and mechanical stability, which determine the performance of the SOFCs. Therefore, understanding the characteristics of the underlying microstructure is of great importance.

The most mature anode material is porous Ni-YSZ, and Ni is the electronic conducting phase, and YSZ is the ionic conducting phase, with additional pores acting as the gas transport medium.[6,7] Critical parameters for the porous anode include three-phase boundary (TPB), tortuosity, phase volume fraction, and pore size diameter.[8] Among these parameters, the tortuosity reflects the resistance effect from the connecting phases (pores, electronic and ionic phase), which account for a certain volume fraction. This resistance effect is established by relating the effective diffusion coefficient (gas, electrons, and ions) in the porous material to the bulk diffusion in free space of the same volume. This resistance effect on gas transport is more obvious, especially at a high current density, where the concentration overpotential dominates the voltage losses.[9] The tortuosity impact on the transport of electrons and ions is important throughout the operation region, especially at the low current density stage where the activation overpotential dominates the voltage loss of the SOFC. Therefore, as long as species transport exists, tortuosity must be considered and treated properly. The tortuosity must first be determined, and therefore a proper calculation and analysis approach is indispensable to accurately relate to the associated transport process.[10,11] However, tortuosity is known as notoriously difficult to calculate due to the intrinsic complexity of the porous medium.[12]

Tortuosity is originally defined as the actual length of the path through a porous material divided by its Euclidean distance (thickness). However, it is not trivial to calculate when considering the complexity of the porous electrode. Different models and assumptions usually need to be made for a specific material. There are literature reviews available dedicated to introducing different definitions of tortuosities.[9,13–15] To summarise, three methods exist to determine the tortuosity. The first one is based on experiments without detailed geometrical information. Diffusion cell model,[16] which applies a pressure-driven diffusion in a porous material to both sides and by measuring the concentration of species on each side to obtain the mass flux. On the basis of different diffusion models such as the Fick model, Dusty Gas Model (DGM) or Maxwell-Stefan model, the effective diffusion coefficient and the tortuosity are obtained. Since concentration overpotential dominates at high current density, the effective diffusion coefficient can be related to the limiting current density, fuel partial pressure, and its molar flow rate.[17] The second and third methods are based on detailed geometric information, with which tortuosity can be

[z]E-mail: xiaoqiang.zhang@energy.lth.se; martin.andersson@energy.lth.se

obtained by the direct path-length finding approach or effective diffusion simulation. The tortuosity is then defined by the actual path length through the percolated pore or solid phase divided by the Euclidean (straight-through) length. Therefore, the so-called spatial tortuosity can be calculated along the diffusion direction. There are several path length-finding approaches, such as distance propagation, the pore centroid method, the fast marching method, and the shortest path search method. For example, Dijikstra's algorithm is used to search for the shortest path from an inlet to the outlet based on a 3D microstructure dataset.[18] The distribution of the tortuosity in the porous material is obtained rather than a single value. There are also path-finding methods directly using the streamlines from the results of CFD simulation.[19,20] The third method uses either voxel or mesh-based simulation on a real 3D microstructure. The voxel-based method can use 2D images only with sufficient resolution to solve diffusion equations through a porous medium.[21,22] The mesh-based method, however, involves mesh generation, and thus mesh quality control is tricky. For example, the finite element method calculates tortuosity by solving partial differential equations (PDE).[23] Apart from these approaches, there are also simpler porosity-tortuosity models to calculate tortuosity, such as the Bruggeman and Maxwell models.[24–26] Among them, the Bruggeman model has a wide range of applications for the flow of porous media in CFD simulations.[27] These methods give a single tortuosity value and the validity used for SOFC electrodes is questionable.[28]

The tortuosity impact on SOFC performance can be reflected by electrochemical impedance spectroscopy. There is a one-dimensional AC and DC model used to analyze the impedance considering homogeneous material properties for diffusion.[29] Experiment test is conducted to investigate the sintering temperature and cathode material infiltration loading impact on polarization.[30] Long-term electrode degradation fed with biomass producer gases is investigated to determine the relevant operating parameters.[31] There is research based on numerical constructed 3D microstructure with low cost and flexibility.[32] The infiltrated electrode material is generated by a random sphere insertion model, and the effective resistance of the electrode is expressed as a function of the microstructure and conductivity of the materials.[33] The Gradient electrode model is constructed numerically to evaluate the tortuosity and fluid flow within it.[34] The cubic-packed 3D electrode model is also used to calculate the tortuosity.[35] The kinetic Monte Carlo (kMC) model is used to investigate the sintering kinetics and microstructure evolution for statistically generated 3D LSM-YSZ electrodes during co-sintering processes.[36] Therefore, the evolution of microstructure properties such as tortuosity is determined.

Over the past decades, advanced technology has been widely applied in the reconstruction of 3D porous material. There are two advanced techniques to obtain 3D tomography of porous material. One is the X-ray computational tomography (CT),[37,38] and the other is the dual beam focused ion beam scanning electron microscopy (FIB-SEM).[39,40] Both obtain detailed high-quality microstructure data. The FIB uses focus Ga^+ ions to cut thin Sections from the exposed electrode surface continuously, meanwhile, the SEM is used to get the images. The sequential cutting and imaging process produces a series of consecutive 2D images of the electrode. The serial 2D images are then processed and used to generate a 3D microstructure of the porous electrode.[41] The rise of such tomography techniques provides new ways to calculate tortuosity using either different path-finding algorithms (path-length-based) or flux-based (CFD) simulations.[14] The multi-scale imaging and modelling method is used to calculate the tortuosity of novel SOFC anode based on X-ray CT.[42] The limiting current density derived tortuosity based on the experiment is compared with random walk diffusion simulation derived one based on 3D real microstructure.[43] The tortuosity factors of the anode are compared between X-ray CT and DRT analysis, which shows good agreement.[44] The time-resolved multiphase-field modelling of nickel coarsening in Ni-YSZ anode is conducted based on FIM-SEM reconstructed microstructure.[45] The high-throughput 3D reconstruction method is used to get the microstructure of infiltrated cathode material based on FIB-SEM followed by analyzing the geometric parameters.[46] The phase field method is used to simulate the Ni-coarsening process based on the 3D microstructure of different anode compositions using FIB-SEM.[47] A 3D Multiphysics coupled dynamic heterogeneous single-cell mode is constructed based on 3D reconstructed cell components using FIB-SEM.[48]

Based on the previous studies, obtaining a real image to accurately reconstruct the analyzed domain is not a common task performed. Meanwhile, the evaluation of different approaches for tortuosity value is still rare. Accurately and correctly determining the tortuosity is necessary for material development and numerical simulation. Therefore, that is the gap filled with the current study. In addition, a combination of real images for digital reconstruction and models for tortuosity computation are key features that provide a much more realistic SOFC anode digital generation. The reconstructed 3D models will be an important input in generating porous electrodes in a process that uses machine learning and artificial intelligence.

In this paper, the difference between each approach for tortuosity will be uncovered by combined experiment, 3D reconstruction and modelling. To do that, different anode microstructure impact on SOFC electrochemical performance is firstly analyzed based on a button SOFC (NiO-YSZ|YSZ|LSM-YSZ|LSM). The microstructure variation is realized by different anode compositions. The material is further used for 2D image collection and reconstruction of the real 3D microstructure. Three different commonly used tortuosity calculation approaches are then compared regarding time, and accuracy. The compared methods are the porosity-tortuosity relationship, path-length-finding approach and voxel-based (flux-based) approach. This paper provides a complete process for cell testing, tomography image generation, 3D reconstruction and tortuosity calculations. The results and their evaluation can provide a reference for tortuosity determination and material optimization.

Experiment

Cell preparation.—The standard procedure for preparing and testing a button SOFC is carried out following the previous work.[49,50] The electrolyte is a YSZ pellet with a thickness of 150 μm and a diameter of 2 cm. Different compositions of NiO-YSZ (60:40 and 40:60 in wt%) with 2 wt% KD1 dispersant (to the total solid ceramic weight) is placed in a plastic jar. The 1 cm diameter milling ball filled 1/3 of the plastic jar is then added with acetone, which immerses the balls followed by milling at a speed of 160 rpm for 24 h. Then, the fully mixed and dispersed solid ceramic particle is poured into a beaker filled with acetone and mixed with a magnetic stirrer. Simultaneously, the organic vehicle (5 wt% Butvar PVB in 95 wt% Terpineol (mixed isomer)) with 33 wt% of the total solid weight is poured into the beaker. The beaker is covered with aluminum foil pierced with small holes to allow acetone to evaporate slowly. After the acetone is fully evaporated, the anode slurry is ready for screen printing. The prepared anode material with 60:40 and 40:60 wt% is then named composition 1 (CP1) and composition 2 (CP2). The anode slurry is screen printed on the electrolyte pellet with a diameter of 1 cm followed by sintering at 1250 °C for 2 h. The estimated thickness of the anode is approximately 20–23 μm.

The LSM-YSZ (50:50 wt%), and LSM slurry are prepared following the same procedure as the preparation of the anode slurry, which consists of KD1 dispersant (2 wt%) and an organic vehicle (33 wt%). The LSM-YSZ (active layer) and LSM (current collect later) slurry are then sequentially screen printed on the opposite side of the anode with a diameter of approximately 0.8 cm, with an effective active area of 0.5 cm^2. The overall thickness of the cathode is in the same order as the anode. The screen-printed cathode is then sintered at 1100 °C for 2 h. Finally, the silver wire is attached to the surface of the anode and cathode with silver paste and sintered at 850 °C for 1 h. The button SOFC unit cell is ready for testing.

Test and characterization.—The cell test configuration is shown in Fig. 1. The cell is attached to the end (right-hand side) of an alumina tube I, which is sealed with a ceramic bond. Additionally, a small alumina tube II is connected to the fuel inlet through a metal tee II with a thermal couple inserted. The other side of tube II is connected to tube I through a metal tee I with one way acting as a fuel outlet. The assembled test kit is then inserted into the programmable tube oven. At the beginning of each test, the NiO in the anode is reduced to Ni at 800 °C using 5% H_2. The reduction is complete when the open-circuit voltage is above 1.0 V. Pure H_2 with a flow rate of 15 ml min^{-1} is used as fuel, while the cathode side is open to the air. The Solartron SI 1280B electrochemical measurement unit is used to obtain voltage and power density vs current density (IVP) curves and impedance. The IVP test sweeps the voltage from the open circuit voltage (OCV) to 0.2 V and then back to OCV with a sweep rate of 5 mV s^{-1}. The EIS frequency ranges from 20 kHz to 0.1 Hz with an AC amplitude of 20 mV. Cells are tested at temperatures of 700 °C, 750 °C, and 800 °C.

After the tests are performed, the cell is disassembled and infiltrated with resin in a low-pressure atmosphere to distinguish the pores and the solids. After resin infiltration, the sample is abraded with abrasive paper (P600 & P1200 grits in the FEPA/ISO 6344 standard). The sample is then polished with diamond polish powder paste of a size of 6 μm and 3 μm sequentially. An FEI Scios Dual Beam instrument was employed for FIB-SEM analysis. Prior to milling, protective Pt layers were deposited using the electron beam (acceleration voltage of 3 kV and nominal current of 13 nA with dimensions of $10 \times 10 \times 0.2$ μm^3) and ion beam (30 kV, 1 nA, $11 \times 11 \times 1$ μm^3). All ion beam milling was performed at an acceleration voltage of 30 kV with initial bulk milling at 65 nA followed by steps at successively decreasing nominal beam currents of 15, 5 and 3 nA.

The SEM and FIB form an angle of 52°. As the FIB cuts away the anode material from the inner trench surfaces, the SEM images are obtained consecutively after each cutting. Depending on the structure of the anode material, the distance between adjacent images is set to 40–50 nm. A total of 208 and 218 images are acquired for CP1 and CP2 respectively. A Section of the original noisy image stack is shown in Fig. 2b. The curtaining effects (i.e. preferential milling) and residual image drift were corrected in post-processing.

3D reconstruction.—The workflow from FIB-SEM to a 3D reconstructed geometry is shown in Fig. 3. The original poor-quality image stack is shown in Fig. 3b. Avizo version 9 (Thermo Fisher Scientific) is used for image processing and 3D reconstruction of porous anode material. The images are aligned using a box mask and cropped to encompass only the porous material, defining the final dimensions of the sample. A Fast Fourier Transformation (FFT) filter is used to remove the directional curtaining artefacts.[51] The Non-Local Means filter is used for denoising followed by segmentation via a watershed threshold.[52] Through this filter, detailed features are reserved without noise pixels. The processed images are processed with a segmentation editor, and during this step, the pores and solids are separated. Isolated pixels smaller than 100 pixels are removed, and this is to remove the isolated pores which are not percolated. Figure 3c shows the image stack after threshold, segmentation and binarization (part of the image stack). Finally, the surface is generated and exported as an STL(stereo lithography) surface mesh file for further simulations. The volume of the 3D porous material CP1 and CP2 is 10 μm × 8 μm × 7μm and 12 μm × 11 μm × 7 μm respectively, as shown in Figs. 3d and 3e, where blue is the pores and green is solid. It can be seen that the pattern has a big difference regarding the distribution of the pores between CP1 and CP2, e.g. there are more percolated and evenly distributed pores for CP1. These results demonstrate that the composition of NiO:YSZ would have a big impact on the formation of a porous network.

The authors noted that the microstructure parameters vary with different representative volume sizes. Increasing the sample volume will naturally improve the statistics at the expense of increased acquisition & computational time.[53] Provided the total volume for both the samples is similar and the pore sizes are also comparable then a comparison of one to the other is reasonable. The tortuosity variation with the increase of domain size is direction-dependent, therefore, tortuosity in different directions is calculated for path-length-based, and voxel-based approaches. The same 2D tomography images and the 3D volumes are used to calculate the tortuosities with different approaches. The 2D tomography images are used to calculate the tortuosity using a voxel-based approach. The 3D volume reconstructed by the 2D images is used in the CFD simulation with a path-finding approach for tortuosity calculation. The domain is cut into 8 parts, and 1/8 of the domain is used for the simulation. Since the voxel-based approach reserves the features of the pores without smoothing. The porosity used in the porosity-tortuosity model is calculated by the voxel-based approach.

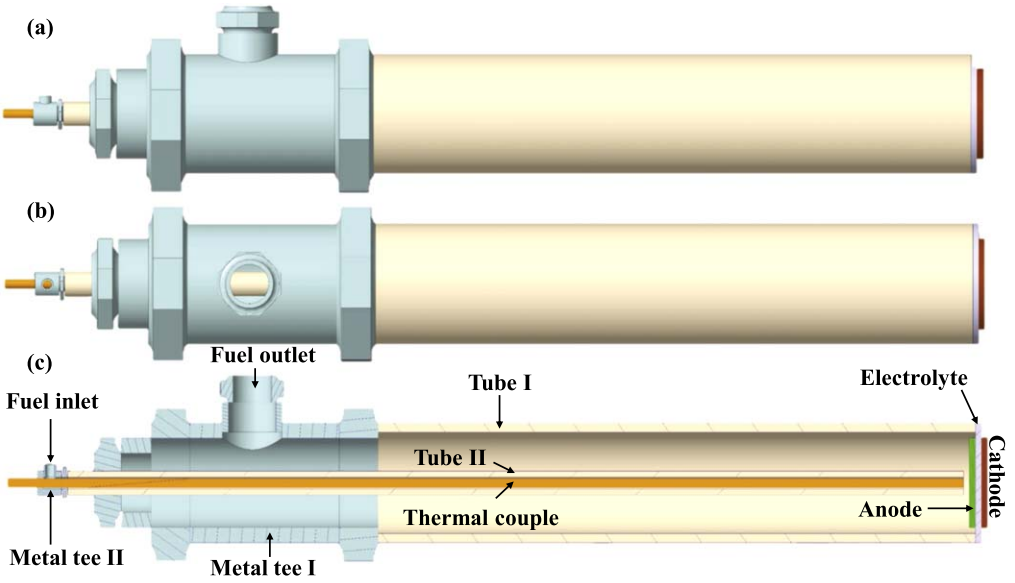

Figure 1. Schematic of the cell test configuration: (a) side view; (b) top view; (c) and cross-section view.

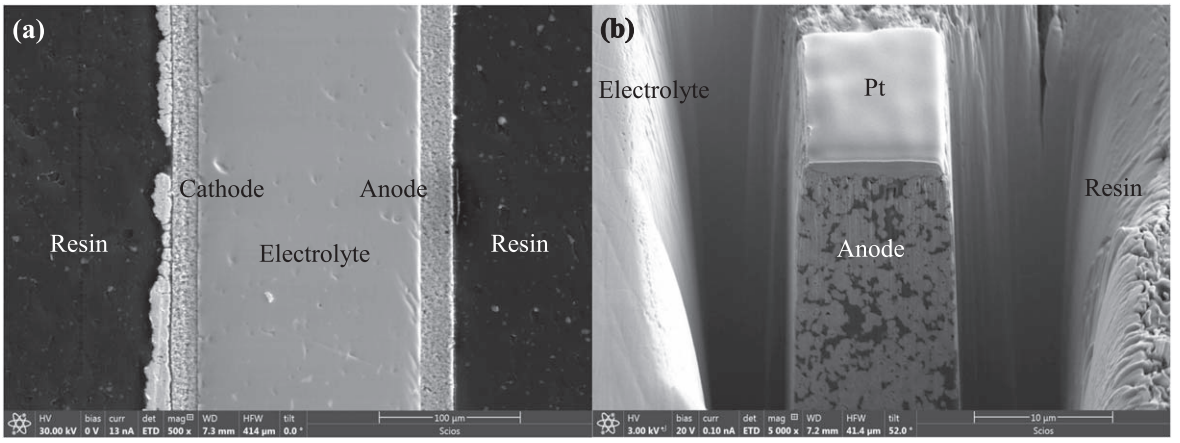

Figure 2. SEM image of (a) cross-section of the polished cell; (b) trench milled on the anode.

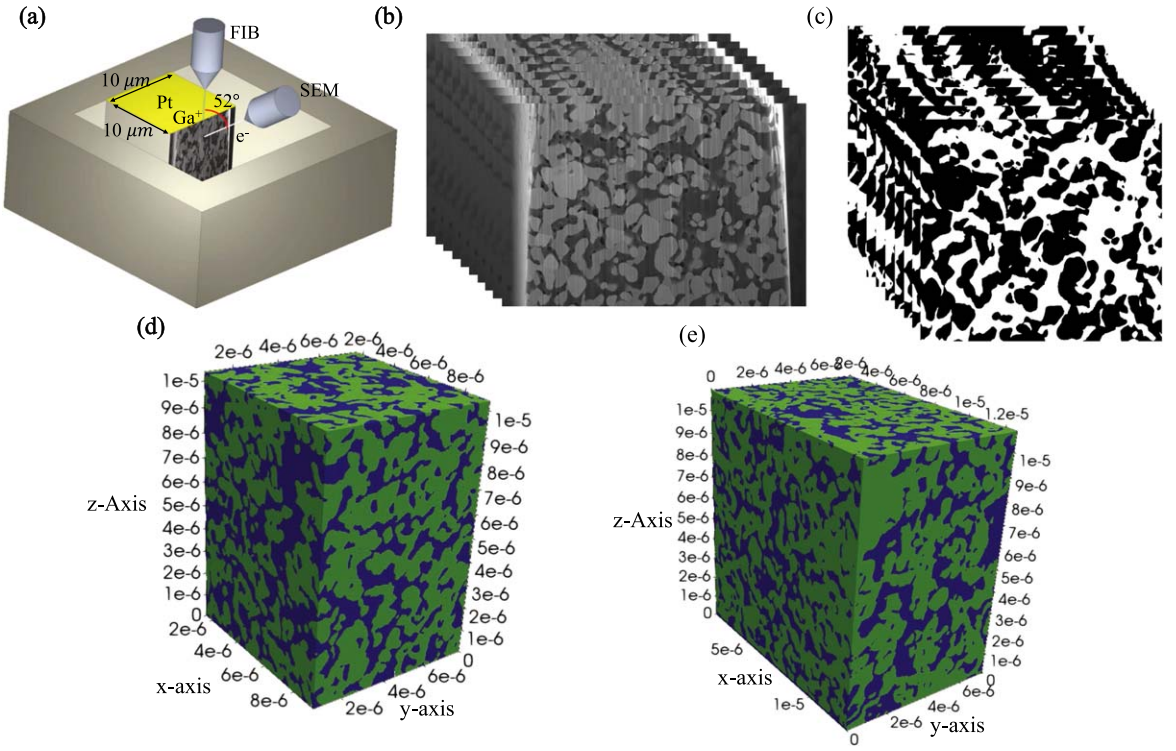

Figure 3. (a) schematic of the FIB-SEM; (b) Original secondary electron images obtained by FIB-SEM; (c) Thresholded images after processing; (d,e) 3D reconstructed porous materials for CP1 and CP2 respectively, the pore is in blue and solid is in green.

Calculations

Definition of tortuosity.—In geometry terms, tortuosity τ is defined as the ratio between the actual tortuous path length (inlet and outlet) Δl, and Euclidean distance (straight through path length between inlet and outlet) Δx. There are different approaches to defining the actual length of the tortuous path. For example, it can be calculated based on the shortest path length,[14] the average path length,[13] and the effective path length (flux-based algorithms).[54] Generally, the geometric tortuosity τ_{geo} is defined as in Eq. 1.

$$\tau_{geo} = \frac{\Delta l}{\Delta x} \quad [1]$$

The geometric definition of tortuosity was originally applied to viscous porous media, which consists of a bundle of sinuous but parallel capillaries or pores. When tortuosity is applied to the diffusive transport of mass, ions and electrons, it reflects the resistance effect of the complex porous medium rather than a simple geometric meaning. Therefore, the effective transport properties ϕ_{eff} and bulk transport properties ϕ_0 are correlated by the dimensionless M-factor to account for the microstructure impact.[55]

$$\phi_{eff} = \phi_0 M \quad [2]$$

There is no universal formula for the M-factor that apply to all porous medium. But the M-factor can be basically related to porosity and tortuosity based on the complexity of the model, such straight-capillary-tube model and the inclined-capillary-tube model, which can be generally expressed as in Eq. 3.[17]

$$M = \frac{\varepsilon^n}{\tau^m} \quad [3]$$

Here m and n are empirical constants. Some models also take into account the constriction factor β and the percolation factor P as

shown in Equation 4.[56]

$$M = \frac{(\varepsilon P)^b \beta^c}{\tau^d} \quad [4]$$

Depending on the different materials, species involved, and diffusion mechanism, the tortuosity may have different values according to corresponding models. Most of the values are single values, which means the material is homogeneous. However, inhomogeneities of the material also suggest that the tortuosity value is coordinate-dependent, which can be obtained through numerical simulations.[54,57] Here, for all calculation approaches in this paper except for the path-length-based approach, we assume that the electrode in each direction is homogeneous.

It is noted that regarding the effective diffusion in a porous media, Epstein differs between tortuosity and tortuosity factor based on a capillary model for pressure drive viscous flow.[58] According to Epstein, failure to distinguish effective pore velocity and the interstitial axial velocity results in tortuosity τ, which should be the square root of tortuosity factor κ. Without considering the difference, the tortuosity is defined according to Eq. 1. However, the definition of the tortuosity factor is controversial, which leads to the definition of the M factor, which is shown in Eqs. 3 and 4. It is important to distinguish between these terms since they are based on different assumptions. By calling "tortuosity τ" in this paper, we adopt the definition coined by Epstein, i.e., tortuosity factor κ, which represents the sinuous but parallel capillaries or pores model. In such a case, the M factor takes the form of Eq. 2. The calculation approach will be introduced in the next section.

Porosity-tortuosity relation.—Without a 3D porous structure, the effective transport of gases and charges in porous material has been derived by diffusion cell experiments and electrochemical measurements based on the appropriate diffusion/transport model as is discussed in the introduction part. Without diffusion cell and electrochemical experiments, one of the most handy methods for the calculation of the tortuosity of a porous material is a porosity-tortuosity correlation. In this paper, three pore-tortuosity models are included and compared.

One of the most widely used is the Bruggeman model,[24,59] as shown in Eq. 5. For a porous medium with a connected conductive phase with an insulating spherical particle of uniform size, the correction factor of $\gamma \approx 1$, and a Bruggeman exponent of $\alpha \approx 1.5$ are used.[14,59]

$$\tau_{Brug} = \gamma \varepsilon^{1-\alpha} \quad [5]$$

It is noted that the Bruggeman correlation is valid when the insulating (obstruction) phase is present in a low volume fraction (saturated porous) and represented by random, isotropic spheres or cylinders.

The Millington and Quirk model also assumes that the porous media is homogeneous and consist of the spherical solid that interpenetrates with each other and spherical pores that also interpenetrate with each other.[60] Besides, there is no cementation and or incomplete dispersion of pore size. The tortuosity in a saturated porous medium can then be expressed as:

$$\tau_{Mill} = \varepsilon^{-1/3} \quad [6]$$

It is noted that for both Bruggeman, Millington and Quirk models, the porous media is assumed to be saturated. For a cluster of randomly arranged spheres, Maxwell's porosity-tortuosity correlation gives the expression as shown in Equation 7.[61]

$$\tau_{Max} = \frac{3 - \varepsilon}{2} \quad [7]$$

Geometric tortuosity.—As shown in Fig. 3, a 3D anode volume is reconstructed using image processing software based on the 2D images obtained by FIB-SEM. The CFD simulation combined path-length-based approach will use 1/8 of the microstructure to perform the simulation. The voxel-based approach utilises the same 2D tomography images to calculate diffusion without meshing. The following Section will show a detailed implementation of both approaches.

CFD simulation combined path-length-based approaches.—The global single value tortuosity can be calculated using the shortest length, the average length, or the effective length (Flux-based algorithms). If the actual length along the flux direction is obtained continuously, the distribution of tortuosity also can be determined starting from the inlet and ending at the outlet. In this paper, three path lengths are determined and used, i.e., minimum, maximum, and average path lengths.

In order to get the fluid flow path length, about 1/8 volume of the constructed domain is used for CFD simulation with the Open FOAM 7.0 software. In addition, the domain is enlarged by 1×10^5, in order to satisfy the CFD simulation criteria and be more robust for mesh generation. The mesh is generated with snappyHexMesh using the same mesh control parameters, such as surface refinement level and mesh quality criteria. The total number of meshes for CP1 and CP2 is 4 M and 1.3 M. The maximum skewness element is within a reasonable range for both cases. For CP1, there are 9 skewed cells with a maximum skewness of 10.72. For CP2, there are 3 highly skewed cells with a maximum skewness of 4.70. There is no aspect ratio, non-orthogonality or other quality error warnings for either case. The Navier-Stokes equations for the steady laminar motion of an incompressible Newtonian-type flow are solved using the SimpleFOAM solver. The SIMPLE algorithm is used to couple the velocity and pressure. The maximum number of iterations for the SIMPLE solver is set to 150. It is noted that thickness direction (x-direction) and radial direction (y-direction) flow are simulated. For the velocity boundary conditions, an inlet velocity of 0.1 m s^{-1} is applied to each inlet, and the outlet is set to zeroGradient. All other surfaces are defined as noSlip boundary conditions. For pressure, the outlet is assigned a fixed value, zero, while all other boundaries are zeroGradient. After simulation, the velocity magnitude streamlines in the porous volume are plotted and exported as a CSV file using ParaView (version 5.6). The CSV file contains the point data (coordination) of each streamline. A simple in-house MATLAB script is developed using MATLAB R2022a coding to process the streamlines. The streamlines are first filtered to eliminate the streamlines with terminal coordination along the flow direction that are less than 5% of the outlet plane coordination. Then, integration is performed on the rest of the streamlines to calculate its length, which represents the species flow path. Finally, the shortest, longest, and average streamlines are determined as the path length to calculate their tortuosity.

Voxel-based algorithms.—Calculation of the tortuosity method proposed by Cooper et al.,[22] is used as the base case. This approach uses processed 2D tomography images directly to calculate the diffusion equations based on the finite difference method. Using such an approach, voxels are used instead of tetrahedral mesh elements to solve the diffusion equations. It should be noted that the mesh is used for CFD simulation, i.e., to obtain the streamlines to find the path length. Basically, the tortuosity is calculated by comparing the diffusion through the porous material F_p with an empty bulk with the same size F_{cv}:

$$F_p = -A_{cv} D \frac{\varepsilon}{\tau} \frac{\Delta C}{L_{cv}} \quad [8]$$

$$F_{cv} = -A_{cv} D_{eff} \frac{\Delta C}{L_{cv}} \quad [9]$$

where D_{eff} is the effective diffusion coefficient, and D is the diffusion coefficient of the empty bulk with the same size. While C is the concentration, A_{cv} and L_{cv} are the cross-sectional area and length of the porous material. The ratio of Eqs. 8 and 9 gives Eq. 10:

$$D_{eff} = D\frac{\varepsilon}{\tau} \quad [10]$$

The tortuosity defined in this expression has a physical meaning and can be related to concentration overpotential through different models.[62] Therefore, the voxel-based approach is taken as the base case. The porosity-tortuosity relation and path-length-based approach on the other hand have a scientific/academic interest. For example, there are mathematical expressions for the porosity-tortuosity relation.[63] Meanwhile, research is done to explore the path-length-based (streamlines) approaches for tortuosity calculations, for example by Pawlowski[19] and Ezzatabadipour.[64] The following boundary equations are applied to solve the equations:

$$\begin{cases} \nabla^2 = 0, & \text{in } \Omega \\ C = 0, & \text{on } T \\ \nabla C \cdot n = 0, & \text{on } I \\ C = 1, & \text{on } B \end{cases} \quad [11]$$

where Ω represents the pores and T, B, and I represent the top, bottom and interface. While n is the outward pointing unit normal to Ω.

Results and Discussions

Testing results.—The EIS plot at different temperatures for CP1 and CP2 anodes is shown in Fig. 4a. It can be seen that the total polarization resistance R_p (difference between real axis intercept) and the ohmic resistance R_s (first intercept with the real axis) decrease with increased temperature for CP1 and CP2, respectively. Besides, for the same temperature, the impedance for CP1 is much lower than for CP2.

From 4 (a), one can see that the high-frequency arc is larger than the low-frequency arc for the CP2 compared with CP1, demonstrating that it is mainly caused by the change of anode composition. The activation polarization impedance contributes to most of the high-frequency response, while the concentration polarization contributes to most of the low-frequency response.[65,66] The high-frequency horizontal-axis intercept R_s for CP1 and CP2 is 0.4 $\Omega \cdot cm^2$ and 1.4 $\Omega \cdot cm^2$ at 800 °C, which is the ohmic resistance of the electrolyte, electrode, and wire respectively. The low-frequency horizontal-axis intercept is 0.7 $\Omega \cdot cm^2$ and 2.8 $\Omega \cdot cm^2$ at 800 °C respectively. Therefore, the total polarization resistance is then calculated as 0.3 $\Omega \cdot cm^2$ and 1.4 $\Omega \cdot cm^2$ for CP1 and CP2, respectively. The increase in resistance for CP2 compared to CP1 at the same temperature is mainly due to the Ni content dropping below the percolation threshold for conductivity.[67,68] The Ni content below the percolation threshold also affects the microstructure of the porous material, as shown in Figs. 3d and 3e, respectively.

The IVP results for CP1 and CP2 are obtained at different temperatures, as shown in Fig. 4b. The OCVs for CP1 and CP2 have the same value, reaching 1.1 V, which is similar to the theoretical value and proves enough hermeticity. It is noted that at low current density, the activation overpotential for CP2 is greater than CP1. This led to a dramatic decrease in cell potential in the activation polarization-controlled area. With the increase in temperature, the OCV decreases for the same composition, which is due to the decrease in Gibbs free energy. Meanwhile, the maximum power density and current density increase for each composition with increasing temperature, which is due to a decrease in the impedance. The maximum power density for CP1 at 800 °C is 379 mW cm^{-2}, while 133 mW cm^{-2} for CP2. The maximum current density at 800 °C for CP1 and CP2 is 1.3 A cm^{-2} and 0.5 A cm^{-2}, respectively. The results at 800 °C of CP1 agree with the experimental test results.[69] The difference in the power density in Fig. 4b for CP1 and CP2 at the same temperature is mainly due to a decrease of percolated Ni in the anode, i.e., the same reason that leads to an increased impedance due to electronic phase decrease. The variation in the composition of NiO-YSZ on cell performance was studied by James et al.,[67] and found that the polarization resistance (R_p) is largely determined by the three-phase boundary density (TPB). However, microstructure parameters such as phase tortuosity and contiguity also have an impact. A contiguous and percolated pathway for mass and charge transport to/from active sites is of great importance. With increasing porosity, the electrical phase as well as the conductivity decrease.[70]

The EIS data with the best performance for CP1 and CP2 at 800 °C are plotted individually with equivalent circuit (EC) fitted curve as shown in Figs. 5a and 5c. The EC model, as in the figure embedded, includes a resistor (R_s) in series with two RQ elements, which include the resistor (R1, R2) and constant phase element (CPE1, CPE2) in parallel. In the EC model, R_s represents the total ohmic resistance of the electrolyte, electrode, and wire, which is the first intercept of the EIS plot with the real axis. The RQ element consists of R1, CPE1 and R2, CPE2 which represents the total polarization arc of the anode and cathode at high frequency and low frequency, respectively.[67] From the zoomed figures, it can be clearly seen that the two semicircle for CP1 is almost equally divided, but the high-frequency arc increased dramatically and the time constant shifted to low frequency. The only change is the anode composition; therefore, it is reasonable to confirm that the high frequency relates to the anode processes.

The EIS curve can only represent the cumulative sum of the polarization components of the different reaction steps at the anode and cathode. The contribution of different polarization resistances may overlap. The convolution equation which connects the distribution relaxation time function to the impedance spectrum Z(ω):[71]

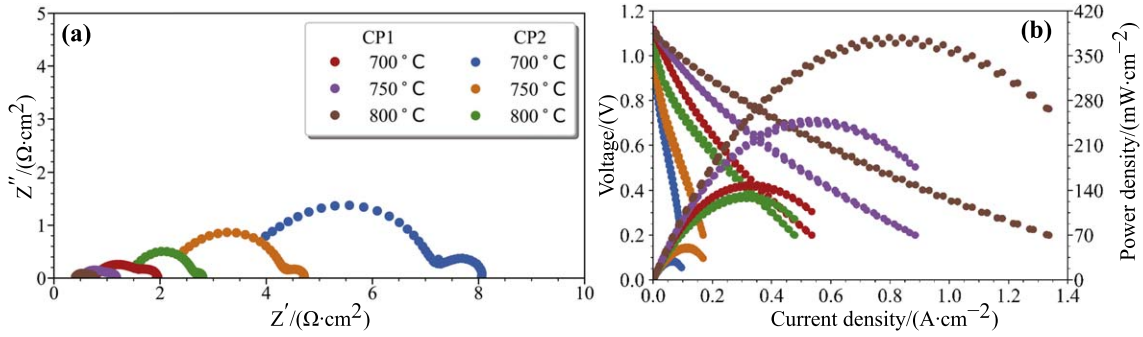

Figure 4. (a) The Nyquist plots measured at 0.7 V for CP1 and CP2 measured at different temperatures; (b) The IVP for CP1 and CP2 at different temperatures. (The same color legend is used for each composition and its testing temperature).

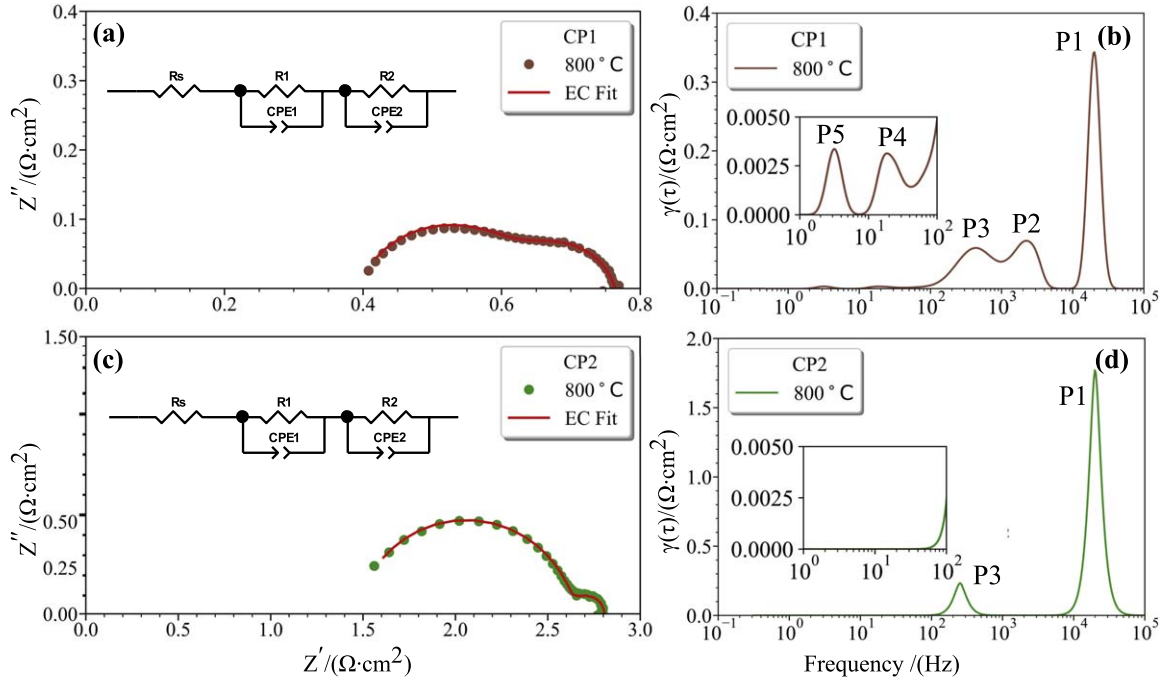

Figure 5. (a), (c) The Nyquist plot and EC fitted curve for CP1 and CP2 at 800 °C; (b), (d) the corresponding DRT curves (frequency between 1–100 Hz is zoomed).

$$Z(\omega) = R_0 + Z_{pol}(\omega) = R_0 + R_{pol}\int_0^{\infty} \frac{\gamma(\tau)}{1 + j\omega\tau} d\tau \qquad [12]$$

where $\gamma(\tau)$ is the distribution of the relaxation times (DRT) and $\int_0^{\infty} d\tau = 1$. The ohmic part (frequency-independent) and the polarization part of the impedance Z(ω) are R_0, $Z_{pol}(\omega)$, and R_{pol} is the polarization resistance. This equation is obtained based on the hypothesis that the underlying physical processes (the impedance) are relaxations. The voltage will eventually be damped out for a current impulse, relaxing monotonically to zero. Therefore, the deconvolution distribution of relaxation times (DRT) can resolve electrode processes with the relaxation times (rate constant) and the relaxation amplitude (loss factors).[72] The different electrochemical processes can be related to different peaks in the DRT plot. The integral area under each peak represents the resistance of each process.

The DRT plots of CP1 and CP2 at 800 °C are shown in Figs. 5b and 5d. It is noted that the relaxation times τ are converted to frequency $f = 1/\tau$. Meanwhile, the DRT fitting-related parameters such as the regularization parameter remain the same. There are five peaks (P1–P5) visible in Fig. 5b for CP1. The high-frequency peak (P1) from 10^3 Hz and 10^4 Hz partially represents the charge transfer at the active three-phase boundary (TPB) in anode.[46] The increase in P1 for CP2 in Fig. 5d is mainly due to the Ni decrease in the anode, and there is a less percolated electronic conducting phase. Therefore, the polarization in the anode is much higher for CP2 than CP1. The second and third peaks (P2, P3) between 10^2 Hz to 10^4 Hz may arise from surface species adsorption/desorption, dissociation, and diffusion.[73,74] The disappearance of P2 may be connected to surface ionic transfer. The surface electronic transfer in the anode decreases due to a decrease in the electronic conducting phase, which can lead to an increase in P3. The low-frequency peak (P4, P5) is mainly due to gas diffusion in the electrode, which in the current case is negligible.[75] The disappearance of P4 and P5 can be attributed to low electrical performance. Although the low electrical performance is mainly caused by Ni decrease, which needs less gas for the reaction, i.e., the current density is not high enough to trigger concentration polarization in CP2. In such a case, other processes such as activation, ohmic polarization, and surface species transport dominate the losses.

Tortuosity.—The porosity—tortuosity relationships just give one value, disregarding the impact of different directions. The tortuosity calculated by the voxel-based approach uses 2D pixel images directly. Therefore, the calculation time is closely related to the number of pixels in the images. In this study, it takes between 2.5 h and 4.3 h for CP1 and CP2 to get the tortuosity, while it takes less than 10 min to run the CFD simulation. The total time consumed for CFD simulation plus the implementation of the path-finding algorithm is much less than the voxel-based approach. The porosity obtained by the voxel-based approach of the CP1 sample is 0.403 and 0.355 for CP2. Considering the circular geometry of the cell, the tortuosity in the thickness direction (x-direction) and radial direction (y-direction) is calculated for the CFD combined path-length-based and voxel-based cases. Meanwhile, the maximum, minimum, and average path lengths are used to calculate tortuosity. For the CFD combined path-length-based finding approach, the velocity profile is presented as streamlines, which represent the actual flow paths. The streamline is then filtered using MATLAB script to account for the path connecting the inlet and outlet.

The enlarged domain which contains only pore structure for the CFD simulation is shown in Figs. 6a and 6d for CP1 and CP2. It can be seen that the pore structures for CP1 and CP2 are different in terms of size, connectivity, and tortuosities from the perspective of each surface. This difference can also be seen in Fig. 3d and 3e, where both solid and pore phases are displayed. The microstructure difference between the two compositions may cause a large performance difference, as discussed before and shown in Fig. 4. The mesh is shown in Figs. 6b and 6e, where the density difference of the mesh is obvious. It should be noted that, as long as the pores are connected and percolated, the mesh is properly generated, and the number of meshes does not affect the final results, which shows the fluid migration through the pores. Therefore, three path length values, i.e., minimum, maximum, and average, are not affected by the mesh number, but by the mesh quality. Bad quality will not only cause divergence of the simulation but also lead to abnormal

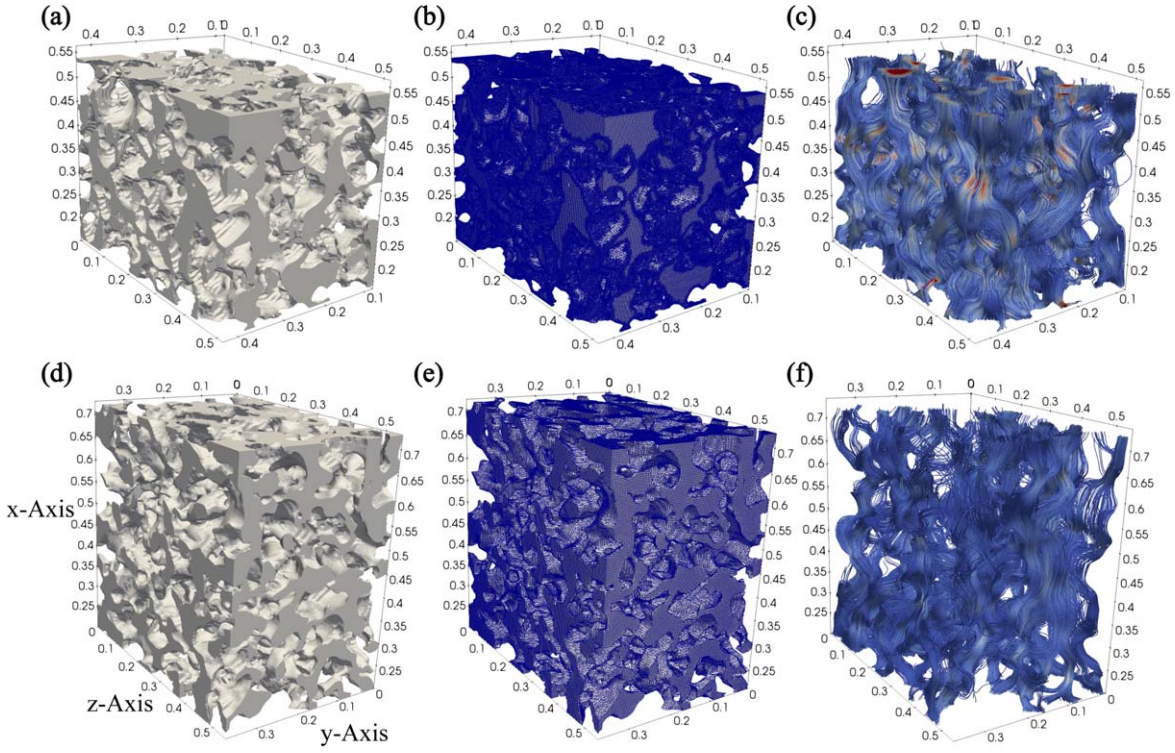

Figure 6. The 1/8 of the original domain for (a) CP1 and (d) CP2; The generated mesh for (b) CP1 and (e) CP2 using snappyHexMesh; The velocity vector streamlines before filtering using MATLAB script in the x-direction for (c) CP1, and (f) CP2.

termination of the streamlines during the progress. As discussed before, the quality of the mesh is satisfactory and without bad quality. Therefore, the simulation results are reasonable and reliable. As can be seen in Figs. 6c and 6f, the velocity magnitude is rendered as a streamline before filtering. There are more streamlines for CP1, which is due to the dense mesh elements, as is described in the calculation method section. Here, we can see that the streamlines are sinuous and parallel, which represent the pore structure. The flow pattern in this manner assumes that the model uses tortuosity rather than tortuosity factor throughout this paper.

To calculate the tortuosity, the Euclidean (straight-through) distance between the inlet and outlet planes is needed. Table I lists the Euclidean length together with different path lengths in the x/y direction after filtering for CP1 and CP2. It is noted that in this study, the size of the domain assumed has no effect on path length. Instead, the Ni content which for CP1 is larger than CP2 definitely has a larger effect compared with the domain size. Since Ni will agglomerate during the reduction process, it will have an impact on the pore distribution and thus affect the minimum, maximum, and average path length. The values in Table I are inserted into Eq. 1 to obtain the tortuosity.

Table II shows the tortuosities values obtained using different calculation methods. It is noted that the voxel-based method in this study is treated as a base case. The porosity for CP1 and CP2 samples are 0.403 and 0.355. All calculation methods show that the sample with a lower NiO content (CP1) has slightly higher tortuosity, regardless of the direction and path chosen. This is in agreement with the general trend of porosity-tortuosity relationships.[25] The EIS in Fig. 5 shows that the low-frequency arc for CP2 is slightly larger than CP1. The difference means that there is a higher concentration overpotential and thus higher tortuosity for CP2 than CP1. The DRT plot for CP1 shows that there are two low-frequency peaks (P4, P5), which corresponds to extremely low concentration losses. However, the low-frequency peaks disappear for CP2, which may be due to the slow reaction rate as the Ni content is below the percolation threshold and the losses are dominated by charge transfer and reactions.

Table I. The Euclidean, maximum, minimum and average path length (×10 μm) for CP1 and CP2 along x (thickness) and y (radial) direction.

	CP1		CP2	
	x (thickness)	y (radial)	x (thickness)	y (radial)
Euclidean	0.36	0.33	0.49	0.35
Minimum	0.41	0.40	0.58	0.41
Maximum	0.72	0.71	0.99	0.82
Average	0.51	0.47	0.72	0.51

For CP1, the tortuosity calculated by both the voxel-based and the CFD simulation combined path-length-based approach shows that there is a small difference in the x-direction (thickness) and the y-direction (radial). However, CP2 has a larger difference in the x- and y-direction. This means that the sample with higher Ni content has better homogeneity. This is due to more percolated Ni, which will be distributed homogeneously in both x- and y-direction. Therefore, the following agglomeration in CP1 compared to CP2 will lead to more homogeneously dispersed pores.

For the voxel-based case, CP1 in the x- and y-direction have a tortuosity of 2.00 and 2.07 respectively. While CP2 have a higher value of 2.44 and 2.29 in the x- and y-directions compared with CP1. The voxel-based approach gives the highest tortuosity among the compared approaches. From Table II it can be seen that among porosity-tortuosity models, Bruggeman gives the highest tortuosity. The tortuosity for CP1 and CP2 is 1.58 and 1.69 respectively. The Maxwell model gives the lowest values of 1.30 and 1.33 for each composition. The Millington and Quirk model value lies between the Bruggeman and Maxwell models with values of 1.36 and 1.41 for CP1 and CP2, respectively. It can be seen that porosity-tortuosity models underestimate tortuosity.

For CFD simulation combined path-length-based approach, the tortuosity is close to the voxel-based approach when choosing the maximum path length. The results show that taking the shortest path

Table II. Tortuosity calculated using different methods; The porosity-tortuosity relationship gives single value; The x-direction (thickness) and y-direction (radial) are calculated for Voxel-based and path-length-based method; The path-length-based method counted minimum, maximum, and average path length.

Method	CP1						CP2					
Brug	1.58						1.69					
Mill	1.36						1.41					
Max	1.30						1.33					
Voxel	2.00			2.07			2.44			2.29		
Path	1.14	2.00	1.42	1.21	2.00	1.42	1.18	2.02	1.47	1.17	2.34	1.46

length to calculate the tortuosity gives small values, e.g., in the x-direction with values of 1.16 and 1.18, in the y-direction, it is 1.21 and 1.17 for CP1 and CP2. Taking the average path length, a value of 1.42 is obtained for CP1 in both directions. The CP2 gives slightly higher values of 1.47 and 1.46 in the x- and y-direction. Therefore, taking the shortest or average path length will lead to an underestimate of tortuosity. However, it is interesting that when taking the maximum path length, the tortuosity is the same as in the voxel-based case in the x-direction for CP1. The y-direction also gives a similar value. CP2 have a tortuosity of 2.02 and 2.34 respectively, which shows the difference in two directions and slightly deviates from the voxel-based approach.

It is noted that the tortuosity according to the different approaches is between 1 and 2.5. This means that the anode material has a rather low concentration overpotential. Since the voxel-based approach is derived from a diffusion model and taken as a standard case. The tortuosity then becomes slightly above 2, which is in accordance with the literature.[76] While the tortuosity for the ionic/electronic phase is usually above 5 or even higher which is due to a higher volume fraction, as is shown in the literature.[47] It is obvious that a higher volume fraction tends to have higher tortuosity for all phases, therefore, further investigation is recommended, e.g., with more broad and fine-tuned compositions.

To clearly see the deviation of different approaches from the voxel-based case, the deviation percentage is further calculated and listed in Table III.

The deviation for each case from the voxel-based approach is listed in Table III. It can be seen that the deviation is composition-dependent, and CP1 deviate smaller than CP2 for all approaches. All methods deviate from the base of more than 20%, except for the one based on maximum path length, for which the deviation is less than 20% for CP1 and CP2. Among porosity-tortuosity models, the Maxwell model deviates most from the base case. The Bruggeman deviates the least from the base case, whereas the Millington and Quirk models lie between the Bruggeman and Maxwell models. Both minimum and average path lengths deviate more than the maximum length, especially for minimum length, which deviates −52% and −49% in the x- and y-direction for CP2. It is noted that the maximum path length derived tortuosity deviates the least from all other approaches, but it seems the deviation is composition dependent. The deviation for CP2 is −17% and −2% in the x- and y-direction for CP2. While CP1 has no deviation and −3% deviation in two directions respectively. This means that the CFD simulation combined path-length-based approach is case-dependent. The large difference in the x- and y-direction for CP2 further uncovers that homogeneity is not good as that of CP1 due to the Ni content below the percolation threshold. The results are different from the literature, which choose minimum or average path length for tortuosity calculation. This difference may arise from the difference between CFD simulation and path-finding approaches such as distance propagation, pore centroid method, and fast marching method.

Table III. Tortuosity in thickness direction for CP1 and CP2 deviation from the base case, i.e., voxel-based tortuosity; The deviations are expressed as a percentage, where negative represents underestimate, and positive overestimation.

Method	CP1			CP2		
Brug	−21%			−31%		
Mill	−32%			−42%		
Max	−35%			−45%		
Path	−43%	0%	−29%	−52%	−17%	−40%
	−42%	−3%	−31%	−49%	−2%	−36%

The results of the CFD simulation combined path-length-based approach agree well with the voxel-based tortuosity when the maximum path length is taken. It should be noted that published studies fail to distinguish between tortuosity and tortuosity factors, and underlying assumptions are different. Epstein clarified the detailed description of the root that led to this confusion.[58] The fluid flow in the porous medium has a low velocity and is significantly lower compared to the gas channel, therefore the Reynolds number is small and the flow is laminar. Therefore, the tortuosity adopted in this paper is reasonable, since the flow is assumed to be parallel. However, it should be noted that this model will not be suitable at high Reynolds number conditions when turbulence occurs. Future work is needed to investigate the relationship between the composition of anode materials and tortuosity. The trade-off point for composition and SOFC performance also needs to be determined.

Summaries

The button SOFCs are assembled and tested, followed by FIB-SEM to obtain 2D images. Both EC fitting and DRT methods are used to analyze the EIS data. For 3D volume reconstruction, the 2D images are first processed by removing the curtain effect, decrease of noise, increase of contrast and cropping. Then the image is segmented according to “solid” and “pores”, and made binary for 3D surface mesh generation. The 2D image is used to calculate the touristy through a voxel-based approach, which is a flux-based approach. The porosity obtained by the voxel-based approach is used in porosity-tortuosity models. Based on the reconstructed 3D volume, the fluid flow in the pores is simulated. The velocity magnitude streamlines are exported for filtering to obtain the path length. The experimental and calculation results can be concluded as follows:

- The sample with a higher YSZ concentration, i.e. CP2, has higher tortuosity, lower porosity and percolated electronic conducting phase than CP1;
- Both IVP curve and DRT analysis of EIS data show that surface and TPB charge transfer processes are greatly decreased due to low Ni percolation for CP2 compared with CP1;
- The Voxel-based method which is defined as a base case, gives the highest tortuosity;
- The most commonly used tortuosity-porosity model such as the Bruggeman and Maxwell model usually underestimates the tortuosity;
- The path-length-based approach with the shortest and average path length gives unrealistically low values. However, the longest

path length gives a value similar to the voxel-based value, which is considered a reasonable value in the current calculation approach.

It is concluded that the low-performance SOFC has higher tortuosity calculated by all methods. The time for CFD simulation combined path-length-based approach is shorter than voxel-based approach, and gives similar value. It is noted that both shortest and average path lengths underestimate the tortuosity like the porosity-tortuosity relationship. A low-value tortuosity means less concentration polarization, which may cause oversimplification of the polarization model to asses the SOFC performance. The longest path length gives comparable value with less time can be an advantage over the time-consuming approaches. However, it should be noted that the path-length-based approach is based on a geometrical definition, which has scientific/academic significance. While the voxel-based approach has a physical significance, which is obtained through an effective diffusion model.

The uniqueness of the paper is to investigate the microstructure impact on SOFC performance and further extract the tortuosity based on 3D reconstructed microstructure. As such, the experiment and simulation/calculation are combined, which uncovers that tortuosity has an impact on SOFC performance. Besides, the difference between the three commonly utilized approaches for tortuosity calculation is investigated. The results are indicative of choosing the tortuosity calculation approach. The procedure of analyzing the impact of microstructure on SOFC performance is promising and offers benefits for optimizing porous electrode architecture.

Acknowledgments

X. Q. Zhang acknowledges the Chinese Scholarship Council (grant number: 201906070189). Great appreciation also from X. Q. Zhang and M. Andersson to the Royal Physiographic Society in Lund for sponsoring a 6 month research stay in the JTSI group at the School of Chemistry at the University of St. Andrews. A.B.N. and J. T.S.I. gratefully acknowledge support from the ESPRC through grants EP/L017008/1, EP/R023751/1 and EP/T019298/1. For the purpose of open access, the author has applied a Creative Commons Attribution (CC BY) licence to any Accepted Author Manuscript version arising.

ORCID

Xiaoqiang Zhang https://orcid.org/0000-0001-6291-8229
Mayken Espinoza-Andaluz https://orcid.org/0000-0001-7809-8659
Tingshuai Li https://orcid.org/0000-0002-9332-9299
John T. S. Irvine https://orcid.org/0000-0002-8394-3359
Martin Andersson https://orcid.org/0000-0001-5057-4908

References

1. K. Kendall and M. Kendall, *High-temperature Solid Oxide Fuel Cells for the 21st Century: Fundamentals, Design and Applications*, ed. K. Kendall and M. Kendall (Boston)(Elsevier) (2015).
2. S. Mukerjee, R. Leah, M. Selby, G. Stevenson, and N. P. Brandon, *Solid Oxide Fuel Cell Lifetime and Reliability* (London)(Elsevier)173 (2017).
3. J. Irvine et al., *J. Phys.: Energy*, **3**, 031502 (2021).
4. P. A. Connor et al., *Adv. Energy Mater.*, **8**, 1800120 (2018).
5. M. Guo, Z. Yang, J. Liu, Y. Jin, X. Wu, F. Chen, and S. Peng, *Ceramics International*, **47**, 14630 (2021).
6. S. Tao and J. T. Irvine, *The chemical record*, **4**, 83 (2004).
7. B. S. Prakash, S. S. Kumar, and S. Aruna, *Renew. Sustain. Energy Rev.*, **36**, 149 (2014).
8. A. Bertei, E. Ruiz-Trejo, K. Kareh, V. Yufit, X. Wang, F. Tariq, and N. Brandon, *Nano Energy*, **38**, 526 (2017).
9. P. Shearing, D. Brett, and N. Brandon, *International Materials Reviews*, **55**, 347 (2010).
10. X. Zhang, M. Espinoza, T. Li, and M. Andersson, *International Journal of Hydrogen Energy*, **46**, 37440 (2021).
11. D. Zhang, A. Bertei, F. Tariq, N. Brandon, and Q. Cai, *Progress in Energy*, **1**, 012003 (2019).
12. B. Tjaden, J. Lane, P. J. Withers, R. S. Bradley, D. J. Brett, and P. R. Shearing, *Solid State Ionics*, **288**, 315 (2016).
13. B. Ghanbarian, A. G. Hunt, R. P. Ewing, and M. Sahimi, *Soil science society of America journal*, **77**, 1461 (2013).
14. B. Tjaden, D. J. Brett, and P. R. Shearing, *International Materials Reviews*, **63**, 47 (2018).
15. J. Fu, H. R. Thomas, and C. Li, *Earth-Science Reviews*, **212**, 103439 (2021).
16. W. He, J. Zou, B. Wang, S. Vilayurganapathy, M. Zhou, X. Lin, K. H. Zhang, J. Lin, P. Xu, and J. H. Dickerson, *Journal of Power Sources*, **237**, 64 (2013).
17. M. J. Martínez, S. Shimpalee, and J. Van Zee, *J. Electrochem. Soc.*, **156**, B80 (2008).
18. A. Cecen, E. Wargo, A. Hanna, D. Turner, S. Kalidindi, and E. Kumbur, *J. Electrochem. Soc.*, **159**, B299 (2012).
19. S. Pawlowski, N. Nayak, M. Meireles, C. Portugal, S. Velizarov, and J. Crespo, *Chemical Engineering Journal*, **350**, 757 (2018).
20. M. Zare and S. H. Hashemabadi, *Chemical Engineering Journal*, **361**, 1543 (2019).
21. A. S. Joshi, K. N. Grew, J. R. Izzo, A. A. Peracchio, and W. K. Chiu, *Journal of Fuel Cell Science and Technology*, **7**, 011006 (2010).
22. S. Cooper, A. Bertei, P. Shearing, J. Kilner, and N. Brandon, *SoftwareX*, **5**, 203 (2016).
23. J. Joos, M. Ender, T. Carraro, A. Weber, and E. Ivers-Tiffée, *Electrochimica Acta*, **82**, 268 (2012).
24. B. Tjaden, S. J. Cooper, D. J. Brett, D. Kramer, and P. R. Shearing, *Current Opinion in Chemical Engineering*, **12**, 44 (2016), Nanotechnology/Separation Engineering.
25. M. Espinoza, B. Sundén, M. Andersson, and J. Yuan, *ECS Trans.*, **65**, 59 (2015).
26. M. E. Andaluz, J. Ávila, J. Pagalo, T. Li, Y. Qi, S. Li, X. Zhang, and M. Andersson, *ECS Trans.*, **103**, 1665 (2021).
27. Chemical Reaction Engineering Module User's Guide, pp. 144-145. COMSOL Multiphysics® v. 6.0. COMSOL AB, Stockholm, Sweden. 2021.
28. D.-W. Chung, M. Ebner, D. R. Ely, V. Wood, and R. E. García, *Model. Simul. Mater. Sci. Eng.*, **21**, 074009 (2013).
29. J. Deseure, Y. Bultel, L. Dessemond, E. Siebert, and P. Ozil, *Journal of Applied Electrochemistry*, **37**, 129 (2007).
30. M. Gibelli, G. Cordaro, and A. Donazzi, *Industrial & Engineering Chemistry Research*, **60**, 6639 (2021).
31. V. Subotić, A. Baldinelli, L. Barelli, R. Scharler, G. Pongratz, C. Hochenauer, and A. Anca-Couce, *Applied Energy*, **256**, 113904 (2019).
32. Y. Zhang, Y. Wang, Y. Wang, F. Chen, and C. Xia, *Journal of Power Sources*, **196**, 1983 (2011).
33. C. Setevich and S. Larrondo, *Electrochimica Acta*, **425**, 140686 (2022).
34. M. Espinoza-Andaluz, M. Andersson, and B. Sundén, *8th International Conference on Applied Energy, ICAE2016, 8-11 October 2016, Beijing, China, Energy Procedia*, **105**, 1332 (2017).
35. W. Kong, Q. Zhang, X. Gao, J. Zhang, D. Chen, and S. Su, *Int. J. Electrochem. Sci*, **10**, 5800 (2015).
36. Y. Zhang, C. Xia, and M. Ni, *International Journal of Hydrogen Energy*, **37**, 3392 (2012).
37. W. Chao, B. D. Harteneck, J. A. Liddle, E. H. Anderson, and D. T. Attwood, *Nature*, **435**, 1210 (2005).
38. J. R. Izzo, A. Joshi, K. Grew, W. Chiu, A. Tkachuk, S. Wang, and W. Yun, *ECS Trans.*, **13**, 1 (2008).
39. J. R. Wilson, W. Kobsiriphat, R. Mendoza, H.-Y. Chen, J. M. Hiller, D. J. Miller, K. Thornton, P. W. Voorhees, S. B. Adler, and S. A. Barnett, *Nat. Mater.*, **5**, 541 (2006).
40. J. R. Wilson, J. S. Cronin, A. T. Duong, S. Rukes, H.-Y. Chen, K. Thornton, D. R. Mumm, and S. Barnett, *Journal of Power Sources*, **195**, 1829 (2010).
41. B. Rüger, J. Joos, A. Weber, T. Carraro, and E. Ivers-Tiffée, *ECS Trans.*, **25**, 1211 (2009).
42. X. Lu, T. Li, O. Taiwo, J. Bailey, T. Heenan, K. Li, D. Brett, and P. Shearing, *J. Phys.: Conf. Ser.*, **849**, 012020 (2017).
43. G. Brus, K. Miyawaki, H. Iwai, M. Saito, and H. Yoshida, *Solid State Ionics*, **265**, 13 (2014).
44. Y. Zhang, Y. Chen, and F. Chen, *Journal of Power Sources*, **277**, 277 (2015).
45. P. W. Hoffrogge, D. Schneider, F. Wankmüller, M. Meffert, D. Gerthsen, A. Weber, B. Nestler, and M. Wieler, *Journal of Power Sources*, **570**, 233031 (2023).
46. Y. Zhang, F. Yan, M. Yan, Y. Wan, Z. Jiao, C. Xia, F. Chen, and M. Ni, *Journal of Power Sources*, **427**, 112 (2019).
47. Y. Xiang, Y. Da, N. Shikazono, and Z. Jiao, *Journal of Power Sources*, **477**, 228653 (2020).
48. Y. Su, Z. Zhong, and Z. Jiao, *Energy & Environmental Science*, **15**, 2410 (2022).
49. R. Price, M. Cassidy, J. G. Grolig, A. Mai, and J. T. Irvine, *J. Electrochem. Soc.*, **166**, F343 (2019).
50. R. Price, U. Weissen, J. G. Grolig, M. Cassidy, A. Mai, and J. T. Irvine, *Journal of Materials Chemistry A*, **9**, 10404 (2021).
51. K. Moreland and E. Angel, *Proceedings of the ACM SIGGRAPH/EUROGRAPHICS conference on Graphics Hardware*112 (2003).
52. A. Buades, B. Coll, and J.-M. Morel, *2005 IEEE Computer Society Conference on Computer Vision and Pattern Recognition (CVPR'05), IEEE***Vol. 2**, p. 60 (2005).
53. J. Laurencin, R. Quey, G. Delette, H. Suhonen, P. Cloetens, and P. Bleuet, *Journal of Power Sources*, **198**, 182 (2012).
54. Y. C Karen Chen-Wiegart, R DeMike, C Erdonmez, K Thornton, S. A Barnett, and J. Wang, *Journal of Power Sources*, **249**, 349 (2014).
55. M. Andersson, S. Beale, M. Espinoza, Z. Wu, and W. Lehnert, *Applied Energy*, **180**, 757 (2016).
56. O. M. Pecho, O. Stenzel, B. Iwanschitz, P. Gasser, M. Neumann, V. Schmidt, M. Prestat, T. Hocker, R. J. Flatt, and L. Holzer, *Materials*, **8**, 5554 (2015).

57. D. Kehrwald, P. R. Shearing, N. P. Brandon, P. K. Sinha, and S. J. Harris, *J. Electrochem. Soc.*, **158**, A1393 (2011).
58. N. Epstein, *Chemical Engineering Science*, **44**, 777 (1989).
59. I. V. Thorat, D. E. Stephenson, N. A. Zacharias, K. Zaghib, J. N. Harb, and D. R. Wheeler, *Journal of Power Sources*, **188**, 592 (2009).
60. R. Millington and J. Quirk, *Trans. Faraday Soc.*, **57**, 1200 (1961).
61. J. Hoogschagen, *Industrial & Engineering Chemistry*, **47**, 906 (1955).
62. S. B. Beale, M. Andersson, C. Boigues-Muñoz, H. L. Frandsen, Z. Lin, S. J. McPhail, M. Ni, B. Sundén, A. Weber, and A. Z. Weber, *Progress in Energy and Combustion Science*, **85**, 100902 (2021).
63. L. Holzer, P. Marmet, M. Fingerle, A. Wiegmann, M. Neumann, and V. Schmidt, *Tortuosity and Microstructure Effects in Porous Media: Classical Theories, Empirical Data and Modern Methods* (Cham, Switzerland)(Springer)p. 51 (2023).
64. M. Ezzatabadipour and H. Zahedi, *Transport in Porous Media*, **136**, 103 (2021).
65. M. Liang, B. Yu, M. Wen, J. Chen, J. Xu, and Y. Zhai, *International Journal of Hydrogen Energy*, **35**, 2852 (2010).
66. N. Shikazono, Y. Sakamoto, Y. Yamaguchi, and N. Kasagi, *Journal of Power Sources*, **193**, 530 (2009).
67. J. R. Wilson and S. A. Barnett, *Electrochem. Solid-State Lett.*, **11**, B181 (2008).
68. N. Q. Minh, *J. Am. Ceram. Soc.*, **76**, 563 (1993).
69. S. Mosch, N. Trofimenko, M. Kusnezoff, T. Betz, and M. Kellner, *ECS Transactions*, **7**, 381 (2007).
70. T. Talebi, M. H. Sarrafi, M. Haji, B. Raissi, and A. Maghsoudipour, *International Journal of Hydrogen Energy*, **35**, 9440 (2010).
71. H. Schichlein, A. C. Müller, M. Voigts, A. Krügel, and E. Ivers-Tiffée, *Journal of Applied Electrochemistry*, **32**, 875 (2002).
72. F. Ciucci and C. Chen, *Electrochimica Acta*, **167**, 439 (2015).
73. Y. Chen et al., *Adv. Energy Mater.*, **7**, 1601890 (2017).
74. C. Sun, Y. Kong, Y. Niu, X. Yin, and N. Zhang, *ACS Appl. Energy Mater.*, **5**, 4486 (2022).
75. V. Sonn, A. Leonide, and E. Ivers-Tiffée, *J. Electrochem. Soc.*, **155**, B675 (2008).
76. D. Kanno, N. Shikazono, N. Takagi, K. Matsuzaki, and N. Kasagi, *Electrochimica Acta*, **56**, 4015 (2011).